High-resolution spectroscopy of neutral Yb atoms in a solid Ne matrix

R. Lambo,[1,*] C.-Y. Xu (徐晨昱),[2,3,*] S. T. Pratt,[4] H. Xu (徐红),[4] J. C. Zappala,[2] K. G. Bailey,[2] Z.-T. Lu (卢征天),[5]
P. Mueller,[2] T. P. O'Connor,[2] B. B. Kamorzin,[6] D. S. Bezrukov,[6,7] Y.-Q. Xie (谢耀钦),[1] A. A. Buchachenko,[6,†]
and J. T. Singh[2,8,‡]
[1]*Shenzhen Institutes of Advanced Technology, Chinese Academy of Sciences, Shenzhen 518055, China*
[2]*Physics Division, Argonne National Laboratory, Argonne, Illinois 60439, USA*
[3]*Department of Physics and Enrico Fermi Institute, University of Chicago, Chicago, Illinois 60637, USA*
[4]*Chemical Science and Engineering Division, Argonne National Laboratory, Lemont, Illinois 60439, USA*
[5]*Hefei National Laboratory for Physical Sciences at the Microscale, CAS Center for Excellence in Quantum Information and Quantum Physics, University of Science and Technology of China, 96 Jinzhai Road, Hefei 230026, China*
[6]*CEST, Skolkovo Institute of Science and Technology, Skolkovo Innovation Center, Moscow 121205, Russia*
[7]*Department of Chemistry, M.V. Lomonosov Moscow State University, Moscow 119991, Russia*
[8]*National Superconducting Cyclotron Laboratory, Michigan State University, East Lansing, Michigan 48824, USA*

(Received 2 July 2021; accepted 16 November 2021; published 16 December 2021)

We present an experimental and theoretical study of the absorption and emission spectra of Yb atoms in a solid Ne matrix at a resolution of 0.025 nm. Five absorption bands were identified as due to transitions from the $4f^{14}5d^06s^2$ $^1S_0$ ground-state configuration to $4f^{14}5d^06s6p$ and $4f^{13}5d^16s^2$ configurations. The two lowest-energy bands were assigned to outer-shell transitions to $6s6p$ $^3P_1$ and $^1P_1$ atomic states and displayed the structure of a broad doublet and an asymmetric triplet, respectively. The remaining three higher-frequency bands were assigned to inner-shell transitions to distinct $J = 1$ states arising from the $4f^{13}5d^16s^2$ configuration and were highly structured with narrow linewidths. A classical simulation was performed to identify the stability and symmetry of possible trapping sites in the Ne crystal. It showed that the overarching $1 + 2$ structure of the high-frequency bands could be predominantly ascribed to crystal-field splitting in the axial field of a 10-atom vacancy of C_{4v} symmetry. Their prominent substructures were shown to be manifestations of phonon sidebands associated with the zero-phonon lines on each crystal-field state. Unprecedented for a metal–rare-gas system, resolution of individual phonon states on an allowed electronic transition was possible under excitation spectroscopy which reflects the semiquantum nature of solid Ne. In contrast to the absorption spectra, emission spectra produced by steady-state excitation into the $^1P_1$ absorption band consisted of simple, unstructured fluorescence bands.

DOI: 10.1103/PhysRevA.104.062809

I. INTRODUCTION

Rare-gas (RG) solids, formed at cryogenic temperatures, are a promising host medium for the capture, detection, and quantum state manipulation of guest atoms and molecules. They provide stable and chemically inert isolation and confinement for a wide variety of guest species at a tunable density, from a single isolated atom to a number possibly exceeding $\sim 10^{16}$ atoms/cm^3. Because RG solids are transparent at optical wavelengths, the guest species can be probed using lasers and the induced fluorescence efficiently detected outside the solid. Spin coherence times of the guest species, which are ultimately dominated by long-range dipolar couplings [1,2], could be made as long as 10^3 s for nuclear spins and 1 s for electronic spins by minimizing spin impurities within the host matrix. Applications of this "matrix isolation" technique include tests of fundamental symmetries [3–5], magnetometry [6,7], and quantum information science [8].

Examples of systems studied specifically for these applications include alkali-metal atoms in both solid RGs [9] and parahydrogen [10], Yb atoms in solid Ne [11,12], and Tm atoms in solid Ar and Kr [13]. For these species, medium effects generally broaden linewidths and shift transition frequencies by several hundred wave numbers [9]. Despite substantial matrix-induced perturbations to their *D* lines, however, alkali-metal atoms have been successfully optically pumped in matrix isolation [6,14]. Furthermore, spin coherence times as long as 0.1 s have been observed for Rb atoms in solid parahydrogen [7].

Ytterbium (Yb) is a heavy divalent atom with a $^1S_0$ electronic ground state, several optical transitions, and a naturally abundant isotope, ^{171}Yb (14%), whose nuclear spin is $\frac{1}{2}$. These features combine to make matrix-isolated ^{171}Yb a promising candidate for a solid-state search for a permanent electric dipole moment [15] or for a nuclear spin-based qubit. Such applications depend on the ability to both optically prepare and read out the ^{171}Yb nuclear spin state. This in turn depends crucially on the strength of the hyperfine interaction

---

[*] These authors contributed equally to this work.
[†] a.buchachenko@skoltech.ru
[‡] singhj@frib.msu.edu

TABLE I. The assignment of the absorption bands appearing in Fig. 3. Here, σ_0 represents the wave numbers of the transitions in vacuum, σ_{abs} the wave numbers of the transitions in solid Ne, and $\Delta\sigma$ the wave-number shifts. The wave numbers are in cm^{-1} with an uncertainty of ±40 cm^{-1} in solid Ne.

Band	Transition	σ_0	σ_{abs}	$\Delta\sigma$
(a)	$6s^2\ {}^1S_0 \rightarrow 6s6p\ {}^3P_1$	17 992	18 510	+518
(b)	$6s^2\ {}^1S_0 \rightarrow 6s6p\ {}^1P_1$	25 068	25 760	+692
(c)	$6s^2\ {}^1S_0 \rightarrow 4f^{13}5d^16s^2\ (7/2, 5/2)_1$	28 857	29 140	+283
(d)	$6s^2\ {}^1S_0 \rightarrow 4f^{13}5d^16s^2\ (5/2, 5/2)_1$	37 415	37 730	+315
(e)	$6s^2\ {}^1S_0 \rightarrow 4f^{13}5d^16s^2\ (5/2, 3/2)_1$	38 422	39 680	+1,260

in the excited state compared to the size of the matrix-induced perturbations. The need to characterize the latter motivates the high-resolution spectroscopic study of Yb atoms in solid Ne (sNe) presented here.

Recent work at relatively low resolution (~0.5 nm) has detailed some of the complexities of Yb/RG systems. When solid Xe was used as the matrix host, absorption and emission bands were found to have a twofold structure due to Yb occupation in tetravacancies and single substitutional sites [16]. Earlier work found that when solid Ar was the matrix host, the same bands had a three-fold structure, due to Yb occupation in hexavacancies, tetravacancies, and single substitutional sites [17]. The symmetry of these trapping sites generally induces crystal-field splitting (CFS) of degenerate atomic states upon excitation [18]. Low symmetries further multiply the number of bands, while high symmetries create secondary structures due to Jahn-Teller electron-phonon coupling [19]. The phonon structure itself is usually not observed, except on certain transitions, forbidden *in vacuo*, of the Mn/Kr [20] and Eu/Ar [21] systems. In the case of bright transitions, the phonon excitations simply contribute to the width of absorption and emission bands.

The above hierarchy of matrix-induced spectral perturbations is typical of the heavy "classical" RG solids made of Ar, Kr, or Xe. In "quantum" matrices, such as those of He and H_2, for which the effects of nuclear motion are expected to be much stronger, the identity of distinct trapping sites is eroded and large-amplitude motions magnify electron-nuclear couplings. Solid Ne is often regarded as a "semiquantum" crystal in which one may expect incipient nuclear quantum effects [22]. At the same time, the Ne crystal is a less perturbing environment than the heavier RGs. Isolated in it, the Yb electronic structure is still qualitatively the same as in vacuum, while the lifetimes of excited states are not significantly different [11,12]. Based on these observations, single-atom detection of Yb in sNe would appear feasible, which could then be extended for use in detecting rare nuclear reactions [23]. This would be in close analogy with the recent demonstration of single-atom imaging of Ba in solid Xe, performed with a view to searching for neutrinoless double-beta decay [24].

In order to investigate all these prospects, we have performed the first high-resolution (0.025-nm) broadband spectroscopy of the low-lying states of the Yb/Ne system (Fig. 1). Five absorption bands were identified as due to Yb atomic transitions from the ${}^1S_0$ ground state of the $4f^{14}5d^06s^2$ configuration to $J = 1$ states of the $4f^{14}5d^06s6p$ or $4f^{13}5d^16s^2$ configuration. These appear as either broad, largely featureless bands or narrow, highly structured ones depending on their susceptibility to the matrix-induced perturbations described above. To assist in their interpretation, we performed classical simulations that gave the structure and symmetry of the Yb/Ne trapping sites and whose corresponding theoretical spectra adequately explained the observed line shapes. The spectrum resulting from steady-state $6s^2\ {}^1S_0 \rightarrow 6s6p\ {}^1P_1$ excitation was also recorded at the same high res-

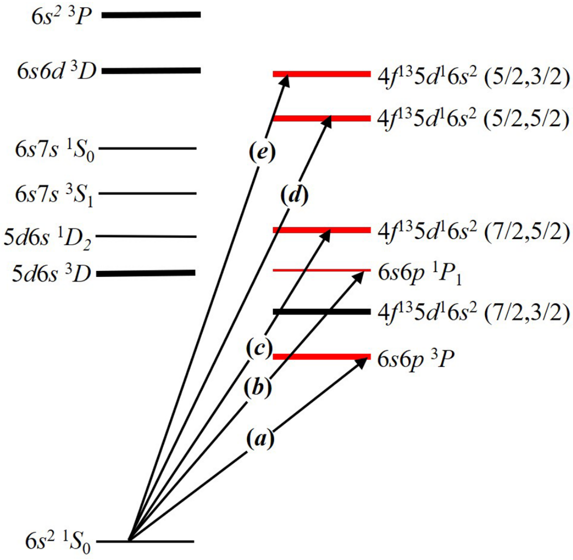

FIG. 1. Low-lying energy levels of the Yb atom with the fine structures omitted. The arrows represent five transitions observed in solid Ne labeled from (a)–(e) following Tables I and II. They correspond to $E1$ transitions from the $6s^2\ {}^1S_0$ ground state to $J = 1$ states in five fine structure manifolds.

TABLE II. The assignment of identifiable emission lines appearing in Fig. 6. Transitions forbidden in vacuum are indicated by the symbol †. Five of the emissions lines are correlated to absorption lines listed in Table I and are labeled with the same letters. Here, σ_0 represents the wave numbers of transitions in vacuum, σ_{emis} the wave numbers of the transitions in solid Ne, and $\Delta\sigma$ the wave-number shifts. The wave numbers are in cm^{-1} with an uncertainty of ±40 cm^{-1} in solid Ne.

Transition		σ_0	σ_{emis}	$\Delta\sigma$
$6s6p\ {}^3P_0 \rightarrow 6s^2\ {}^1S_0$	$(i)^\dagger$	17 288	17 730	+440
$6s6p\ {}^3P_1 \rightarrow 6s^2\ {}^1S_0$	$(ii)/(a)$	17 992	18 320	+320
$6p^2\ {}^3P_1 \rightarrow 6s6p\ {}^1P_1$	(iii)	18 737	18 900	+160
$6s6p\ {}^3P_2 \rightarrow 6s^2\ {}^1S_0$	$(iv)^\dagger$	19 710	20 080	+370
$4f^{13}5d^16s^2\ (7/2, 3/2)_2 \rightarrow 6s^2\ {}^1S_0$	$(v)^\dagger$	23 189	23 070	−120
$6s5d\ {}^3D_1 \rightarrow 6s^2\ {}^1S_0$	$(vi)^\dagger$	24 489	24 490	~0
$6s6p\ {}^1P_1 \rightarrow 6s^2\ {}^1S_0$	$(vii)/(b)$	25 068	25 320	+250
$6s5d\ {}^1D_2 \rightarrow 6s^2\ {}^1S_0$	$(viii)^\dagger$	27 678	27 860	+180
$4f^{13}5d^16s^2\ (7/2, 5/2)_1 \rightarrow 6s^2\ {}^1S_0$	$(ix)/(c)$	28 857	29 030	+170
$4f^{13}6s^26p\ (7/2, 3/2)_2 \rightarrow 6s^2\ {}^1S_0$	$(x)^\dagger$	35 197	35 590	+390
$4f^{13}5d^16s^2\ (5/2, 5/2)_1 \rightarrow 6s^2\ {}^1S_0$	$(xi)/(d)$	37 415	37 730	+320
$4f^{13}5d^16s^2\ (5/2, 3/2)_1 \rightarrow 6s^2\ {}^1S_0$	$(xii)/(e)$	38 422	39 610	+1190

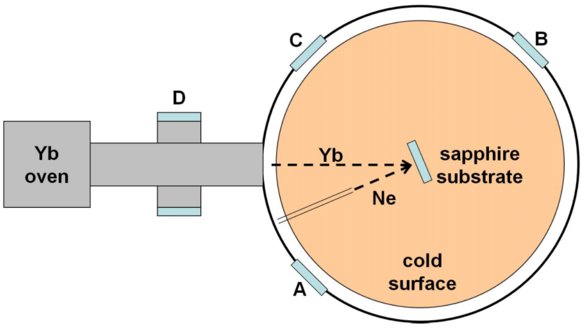

FIG. 2. A sketch of the cold surface inside the liquid-helium cryostat together with the effusion oven and Yb beam line. A, B, and C are three view ports covered with fused silica windows. D is a six-way cross where the Yb beam intensity is measured.

olution. Knowledge of the decay paths originating from the excited singlet state will be important for single-atom spectroscopy.

The remainder of this paper is organized as follows. Section II details the experimental methods, while Sec. III presents the results. These results, together with the classical simulations, are discussed in Sec. IV. A summary and concluding remarks are made in Sec. V.

II. EXPERIMENTAL SETUP

All the experiments were conducted with the liquid-helium cryostat illustrated in Fig. 2. Its cold surface has an area of 300 cm^2 that is cooled by the liquid-helium bath to 4.2 K, at which temperature the pressure of the vacuum falls below 10^{-8} Torr. The Yb/Ne samples were grown on a 2.54-cm-diameter *c*-plane sapphire substrate installed vertically on the cold surface using a copper mount. Indium wires and low vapor pressure grease (Apiezon N) were used to achieve good thermal contact between the substrate and the cold surface. The temperature of the substrate was measured by a resistance temperature detector (Lakeshore CX-1050-AA) and was typically at 4.2–5.0 K depending on the thermal contact.

There were four 2.54-cm-diameter ports on the perimeter of the cryostat. One port was connected to an effusion oven whose crucible was loaded with metallic Yb of natural isotope abundance. The other three ports (A, B, and C in Fig. 2) were closed with fused silica windows and used as view ports. View ports A and B, which were each at an angle of 22.5° to the normal direction of the substrate surface, were used during measurements of the sample thickness and the absorption spectroscopy. View port C, which was at an angle of 67.5° to the normal direction of the substrate surface, was used in the emission study to collect fluorescence from the sample upon excitation.

When preparing the sample, a layer of pure sNe was first grown. The Ne gas flowed through a purifier (LDetek LDP1000) and a 77-K charcoal trap and then leaked into the cryostat via a capillary tube that ended 5 cm away from the substrate. The thickness of the crystal was determined by recording the transmitted light of a He-Ne laser and counting the fringes due to the thin-film interference effect. To preserve its transparency, the sNe growth rate was slowly ramped up to 0.25 μm/h over the first hour, 10 μm/h over the second hour, and finally 50 μm/h over the last half-hour. Once the latter growth rate was reached, the Yb atoms were simultaneously implanted by directing the beam from the effusion oven at the substrate. The crystal could be grown for another five hours before it cracked under its own internal strain.

The Yb intensity was measured using the cross-beam-fluorescence method at the six-way cross (view port D in Fig. 2). A 398.9-nm laser beam resonant with the Yb $6s^2\ {}^1S_0 \rightarrow 6s6p\ {}^1P_1$ transition in vacuum was applied perpendicularly to the Yb beam and the fluorescence measured using a photomultiplier tube along an axis perpendicular to both beams. We found empirically that Yb$_n$ ($n \geqslant 2$) aggregates were negligible and individual Yb atoms were preferentially isolated when the Yb:Ne ratio was kept below 5 ppm. In practice, we held that ratio at 1 ppm for which a Yb beam intensity of 4×10^{14} atoms/cm$^2 \cdot$ h and an oven temperature of 620 K were required. Under these conditions, the Yb areal and volumetric densities were estimated to be 2×10^{15} atoms/cm^2 and 10^{16} atoms/cm^3, respectively. The heat load due to the blackbody radiation of the oven and the deposition of Ne were found to increase the substrate temperature by no more than 50 mK.

In the absorption study, a weak broadband light source (Ocean Optics DH2000-DUV) illuminated the sample through view port A, and the transmitted light was collected through view port B and fiber coupled to a spectrometer. In the emission study, a light-emitting diode (LED) centered at 385 nm illuminated the sample through view port A, and the induced fluorescence was collected at view port C and also fiber coupled to a spectrometer. Two spectrometers were available to us to analyze the absorption and the emission signals, both of which used line CCD cameras as the detectors. The Ocean Optics USB4000-UV-VIS spectrometer covered a broad range from 200 to 1100 nm and had a resolution of 1.5 nm. The McPherson 225 spectrometer had a resolution of 0.025 nm and a range of 200 to 600 nm but with a camera frame that was only 40 nm wide.

To obtain the highest possible spectral resolution, we also used an optical parametric oscillator (OPO) (Continuum Sunlite EX) as the probe light. The OPO was pumped by the third harmonic of a pulsed Nd:YAG laser (Continuum Powerlite DLS) before passing through a frequency doubler (Inrad Autotracker II) to provide UV light. Each pulse was about 10 ns long and contained about 1 mJ of energy. The light was attenuated by four orders of magnitude to avoid melting the sample and damaging the detector. The output beam was split into a probe beam that had a waist at the sample of 1 cm and a reference beam that traveled outside the cryostat. The linewidth of the OPO was about 1 GHz and the frequency was scanned in 2-GHz steps to map out the line shape of the whole absorption band.

III. RESULTS

A. Probe with broadband light

Figures 3 and 4 show the white-light absorption spectra of a typical sample taken, respectively, with the 1.5-nm resolution Ocean Optics and 0.025-nm McPherson spectrometers. Sam-

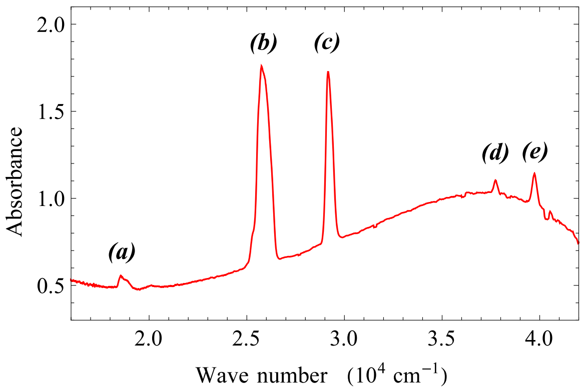

FIG. 3. The absorption spectrum of Yb atoms in solid Ne taken by the Ocean Optics spectrometer with 1.5-nm resolution. All five absorption peaks are identified as Yb atomic transitions from the ground state. See Table I for details.

ple deposition leads to a decrease in the transparency of the substrate which manifests itself as frequency-dependent distortions in the baselines. Nonetheless, five absorption bands, represented in terms of absorbance [25], can be clearly seen and are identified as due to electronic transitions originating from ground-state Yb atoms. Given that the configuration of the ground state is $4f^{14}5d^06s^2$, low-lying excitations can either be $6s \rightarrow 6p$ outer-shell transitions or $4f \rightarrow 5d$ inner-shell transitions, the latter of which break the full $4f$ shell and leave the $6s$ shell intact. In the spectra, bands (a) and (b) correspond to outer-shell transitions whose final levels are $6s6p\ ^3P_1$ and $6s6p\ ^1P_1$ respectively. In contrast, bands (c), (d), and (e) correspond to inner-shell transitions and their final states are $[4f^{13}]_{j_1}[5d^1]_{j_2}6s^2$ in the jj coupling scheme with $(j_1, j_2)_J$ equal to $(7/2, 5/2)_1$, $(5/2, 5/2)_1$, and $(5/2, 3/2)_1$, respectively. A comparison between the wave numbers of transitions in vacuum and those in sNe is summarized in Table I.

Band (a), assigned to the intercombination $6s^2\ ^1S_0 \rightarrow 6s6p\ ^3P_1$ transition, was not observed in our earlier work but becomes visible here due to an increase in the Yb areal density by an order of magnitude [11]. Another difference is in our reassignment of band (d). Recent spectroscopic data and calculations of free Yb atoms [26–28] indicate that it should be associated the $4f^{13}5d^16s^2\ (5/2, 5/2)_1$ state rather than, as previously thought, the $4f^{13}5d^26s^1$ one. In the case of band (e), there was also some ambiguity in its assignment originally. In earlier work it was assigned to to the excited $6s7p\ ^1P_1$ level, the energy of which is 40 564 cm^{-1} above the ground state in vacuum [29]. This implies a redshift in its transition frequency in sNe that is peculiar given that the other four transitions are all blueshifted and makes the narrowness of its peaks inconsistent with the typical effects of the matrix on an $s \rightarrow p$ transition. Reassigning it to the $4f^{13}5d^16s^2\ (5/2, 3/2)_1$ level removes these inconsistencies, though at the cost of a larger-than-expected absolute shift.

In matrix isolation, outer-shell and inner-shell transitions have different line shapes due to the screening of medium effects by the outer-shell electrons [29]. For Yb in sNe, the difference can be readily seen by comparing bands (a) and (b) $(6s \rightarrow 6p)$ with bands (c), (d), and (e) $(4f \rightarrow 5d)$ at the higher spectral resolution of Fig. 4. Band (a) has two principal structures with maxima at 18 530 and 18 826 cm^{-1}, while band (b) has three principal structures with maxima at 25 525, 25 724, and 25 774 cm^{-1}. Although both bands (a) and (b) display some splitting, the linewidth of each peak remains a few hundred wave numbers. By contrast, bands (c), (d), and (e) have more complex structures in which the narrowest linewidth is comparable to the instrument resolution. The three principal structures in band (c) have their peaks at 28 984, 29 049, and 29 073 cm^{-1}. In band (e) there are two clear peaks at 39 631 and 39 652 cm^{-1} and an unresolved shoulder extending from 39 580 to 39 610 cm^{-1}. In band (d) we have a distinct doublet with peaks at 37 741 and 37 751 cm^{-1} and a series of smaller peaks constituting a substructure that extends to lower frequencies.

In the subsequent sections, we propose that the principal peaks of these latter bands are connected to zero-phonon lines (ZPLs) on individual crystal-field levels. We also propose that substructures on these bands are the manifestations of phonon excitations that produce the phonon sidebands typically associated with ZPLs, of which band (d) offers a prime example.

B. Probe with laser light

In order to investigate further the vibronic progression seen in band (d), the $6s^2\ ^1S_0 \rightarrow 4f^{13}5d^16s^2\ (5/2, 5/2)_1$ transition was probed at 2-GHz resolution using frequency-doubled light from the OPO. Figure 5 shows a plot of the absorbed fraction of the incident light intensity (or absorptance α) versus wave number [25]. As with the original white-light spectra, the two peaks centered at 37 741 and 37 751 cm^{-1} were assigned to the $4f^{13}5d^16s^2\ (5/2, 5/2)_1$ state. Extending to lower frequencies, between 37 631 and 37 733 cm^{-1}, one can see a series of nine smaller, consecutive peaks. Possible explanations for this series include multiple site occupancy and/or CFS. However, both of these seem unlikely in this case. First, there is no analogous structure in bands (c) and (e), which indicates that this is a phenomenon peculiar to the $4f^{13}5d^16s^2\ (5/2, 5/2)_1$ transition. Second, attributing this series to multiple site occupancy would require the existence of too many additional trapping sites: at least three of axial symmetry, given that CFS gives rise to three features for each $J = 1$ state; and at most nine, if we assume a one-to-one correspondence between the peaks and trapping sites. This is unsupported by the theoretical calculations of Sec. IV A, while the regularity of the peaks, a spacing of 14 cm^{-1} for the first four, has never been observed in other cases of multiple site occupation.

Instead, we interpret the harmonic series of Fig. 5 as evidence of coupling between the electronic transition and a small number of local phonon modes. This type of structure is usually not visible in RG matrices as electronic transitions tend to couple to a large number of lattice modes to produce an unstructured broadening of the bands in the spectra. In ionic crystals, the emergence of strong vibronic sidebands in transitions involving the upper 4f^N states is associated with strong configuration interaction and coupling to charge transfer states involving ligand electron orbitals [30]. These mechanisms likely also operate here since the large crystal-field splitting observed in the Yb/Ne system is symptomatic of the interplay

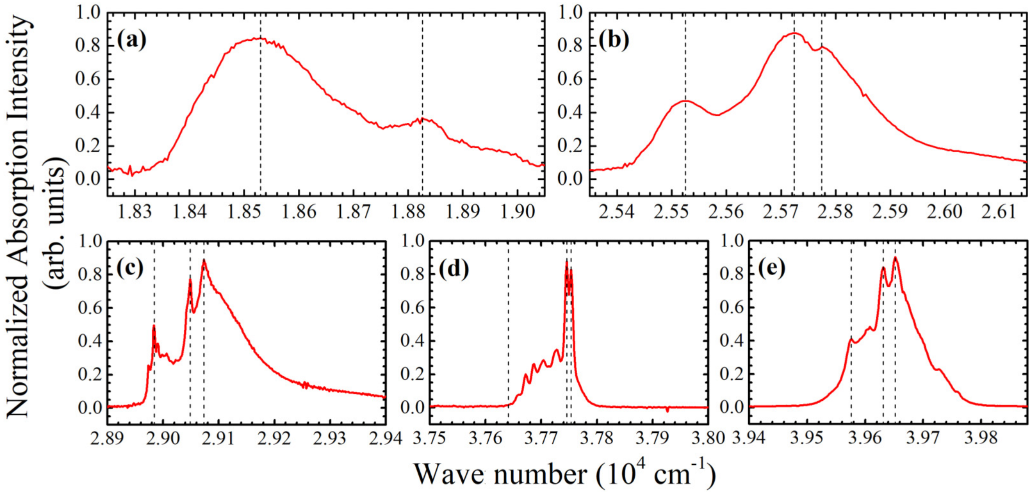

FIG. 4. The detailed line shapes of the absorption bands shown in Fig. 3, registered using the McPherson spectrometer at 0.025-nm resolution. The labels (a)–(e) are the same as those used in Table I. All the panels use the same wave-number scale and the absorption strengths are separately normalized. The positions of the peaks discussed in the text are indicated by dashed vertical lines.

between interelectronic repulsion in the metal atom and the repulsion between the metal electrons and the electron density of the ligands [20].

In the most common treatment, the strength of the electron-phonon coupling is measured by the Huang-Rhys parameter S, which is related to the displacement in the lattice equilibrium position near a defect site Δ accompanying an electron transition according to

$$S = \frac{4\beta^2}{(1+\beta^2)^2}\frac{\omega M\Delta^2}{2\hbar},\ \beta^2 = \frac{\omega'}{\omega}, \tag{1}$$

for which ω and ω' are the frequencies of the vibrational mode in the initial and final electronic states, respectively, and M is the effective mass of the defect site. At very low temperature (i.e., $\hbar\omega > kT \sim 2.8$–$3.5\ \text{cm}^{-1}$) vibronic transitions can be approximated as arising from the zero-phonon ($n = 0$) state and p_n, the probability that the nth vibrational state is populated, can be straightforwardly shown under the Franck-Condon approximation to obey $p_n(S) \propto \exp(-S)S^n/n!$ which is also the form of the overall envelope of the vibronic band [31]. Within that band, on the assumption that coupling involves a single vibrational mode and that the frequencies of the oscillators follow a Gaussian distribution around the mode's average frequency ω, the intensity function of the phonon line n is [32]

$$f_n(E) = \exp(-S)\frac{S^n}{n!} \times \frac{1}{\sqrt{2\pi n\sigma^2}}\exp\left(\frac{-[E-(E_0+n\hbar\omega)]^2}{2n\sigma^2}\right), \tag{2}$$

for which $\sigma\sqrt{n}$ is its linewidth and E_0 is the energy difference between the initial and final electronic states.

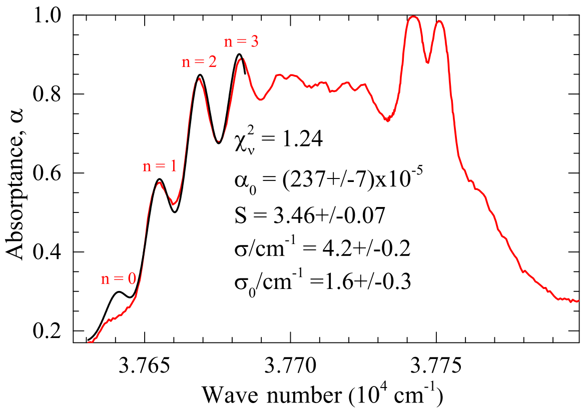

FIG. 5. Ratio of the absorbed to incident light intensity (i.e., the absorptance α) for the $6s^2\ ^1S_0 \rightarrow 4f^{13}5d^16s^2\ (5/2, 5/2)_1$ transition using the frequency-doubled OPO as the probe light. The spectrum has a resolution of 2 GHz. The parameters obtained by using Eq. (3) to fit the first four features of the vibronic band, indicated by the black line, are given in the inset.

We therefore expect to see a harmonic progression in the absorption spectrum in intervals of $\hbar\omega$ and, in Fig. 5, the three phonon lines corresponding to $n = 1, 2, 3$ can be clearly distinguished, centered at 37 655, 37 669, and 37 683 cm^{-1}, respectively. Per Eq. (2), the $n = 0$ order corresponding to the ZPL should be a δ function. In reality, because of electronic dispersion and inhomogeneous broadening due to trapping site inhomogeneity it has a finite width σ_0. Higher-order ($n > 3$) phonon lines are also visible in the range of 37 690 to 37 733 cm^{-1}, though they are not so easily resolved, possibly because the single-phonon approximation no longer holds and interference between multiple modes should be considered. For the sake of simplicity, we only fit the $n = 0$–3 orders using a function for the absorbed fraction of the incident light $\alpha(E)$, that superimposes the ZPL on the single-frequency mode harmonic progressing band [33]:

$$\alpha(E) = \alpha_0\sum_{n=0}^{n=3}\exp(-S)\frac{S^n}{n!}\left(\frac{E_0+n\hbar\omega}{E_0}\right) \times \frac{1}{\sqrt{2\pi(\sigma_0^2+n\sigma^2)}}\exp\left(-\frac{[E-(E_0+n\hbar\omega)]^2}{2(\sigma_0^2+n\sigma^2)}\right) + O. \tag{3}$$

The small fixed offset $O = \alpha(E = 37\,630\ \mathrm{cm}^{-1}) = 0.1703$ accounts for the nonzero background in Fig. 5 produced by light scattered from the matrix. The same figure gives the phonon and ZPL frequencies as $\omega = 14.0\ \mathrm{cm}^{-1}$ and $E_0 = 37\,641\ \mathrm{cm}^{-1}$, respectively. The black trace shows that the fit was performed in the range of 37 630 to 37 685 cm^{-1} and gives the following values for the parameters: $\alpha_0 = (237 \pm 7) \times 10^{-5}$, $S = 3.46 \pm 0.07$, $\sigma_0 = 1.6 \pm 0.3\ \mathrm{cm}^{-1}$, and $\sigma = 4.2 \pm 0.2\ \mathrm{cm}^{-1}$. The lattice displacement Δ can be calculated using Eq. (1) under the approximations that $\beta \simeq 1$ (i.e., $\omega \simeq \omega'$) and M is equal to the sum of the masses of the Yb atom and its nearest-neighbor Ne atoms. We thus obtain $\Delta = 1.29 \pm 0.01$ Å, which is approximately 25% of the ground-state Yb–Ne bond length. This displacement is quite realistic and supports our value for S. It can be easily seen that the fit is least accurate for the $n = 0$ feature. The ZPL at $E_0 = 37\,641\ \mathrm{cm}^{-1}$ is only minimally visible because its intensity is reduced in favor of the phonon sideband. Lower temperatures should make the ZPL more prominent. The maxima of the peaks at 37 741 and 37 751 cm^{-1} cannot be completely discerned due to saturation of the detector. However, their sharpness in Fig. 4(d) strongly suggests that they are also ZPLs on nondegenerate crystal-field levels as discussed more fully in Sec. IV C.

C. Emission spectroscopy

In earlier work, we showed that strong fluorescence of Yb atoms trapped in sNe can be induced by driving the $6s^2\ {}^1S_0 \rightarrow 6s6p\ {}^1P_1$ transition [12,34]. Both a 1-MHz linewidth laser centered at 388 nm (25 770 cm^{-1}) and a 10-nm linewidth LED centered at 385 nm (25 970 cm^{-1}) were able to resonantly excite this transition. This results in a significant population transfer to the metastable $6s6p\ {}^3P_0$ level via $6s6p\ {}^1P_1 \rightarrow 6s5d\ {}^3D_J$ intersystem crossing, the branching ratio of which is enhanced by level mixing induced by the crystal field of the matrix. Due to the long lifetime of the $6s6p\ {}^3P_0$ state in sNe, excited Yb atoms continue absorbing photons to make transitions from this state to even higher excited ones. A strong absorption peak centered at 26 740 cm^{-1}, corresponding to the $6s6p\ {}^3P_0 \rightarrow 6p^2\ {}^3P_1$ excitation, has been previously reported [11]. Given the broad linewidths of absorption peaks in the solid state, the 385-nm LED can also excite this transition and emission from states at higher energies than the exciting photons are thus observed.

Figure 6 shows the full steady-state emission spectrum of Yb atoms in sNe excited by the 385-nm LED and recorded at a resolution of 0.025 nm. We divide the emission lines into the three wave-number regions given below and summarize those we were able to identify in Table II.

Region 1 ($1.7 \sim 2.1 \times 10^4\ \mathrm{cm}^{-1}$). The prominent emission lines in this region are responsible for a green glow from the sample when its is pumped by the LED. They include the decays of the fine-structure triplet group $6s6p\ {}^3P_{0,1,2} \rightarrow 6s^2\ {}^1S_0$ whose spacing in sNe is approximately the same as in the free atom. Although metastable in vacuum, the $6s6p\ {}^3P_{0,2}$ levels decay radiatively in matrix isolation due to a Stark-type mixing induced by the crystal field. The assignments of the $6s6p\ {}^3P_{0,1}$ states have been validated by lifetime measurements in earlier work [12]. It should be noted that the strong emission line at 18 900 cm^{-1} does not belong to this triplet group but corresponds to the $6p^2\ {}^3P_1 \rightarrow 6s6p\ {}^1P_1$ decay following the $6s6p\ {}^3P_0 \rightarrow 6p^2\ {}^3P_1$ excitation mentioned above [11]. The emission line at 20 710 cm^{-1} is the most prominent one that remains unidentified in this region.

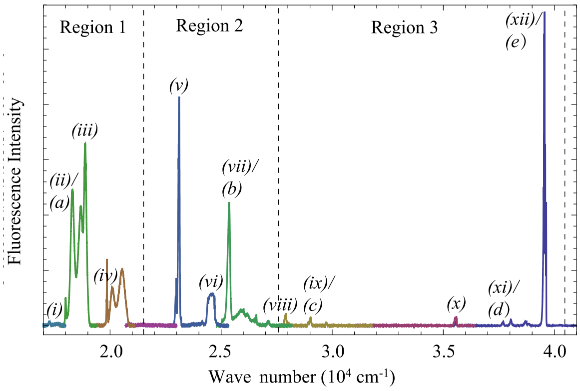

FIG. 6. The steady-state emission spectrum of Yb atoms in solid Ne induced by the 385-nm LED and recorded using the McPherson spectrometer at 0.025 nm resolution. The extent of each color represents the extent of the camera frame. The labels on the identified emission lines are the same as those used in Table II.

Region 2 ($2.2 \sim 2.6 \times 10^4\ \mathrm{cm}^{-1}$). Aside from the $6s6p\ {}^1P_1$ decay at 25 320 cm^{-1}, two strong emission lines are seen in this region. We tentatively propose that the line at 23 070 cm^{-1} corresponds to the decay of the $4f^{13}5d^16s^2\ (7/2, 3/2)_2$ state. This excited level has the same electronic configuration as those of absorption peaks (c), (d), and (e), but the jj coupling of $j_1 = \frac{7}{2}$ and $j_2 = \frac{3}{2}$ does not give $J = 1$ and its decay is thus forbidden in vacuum. This assignment results in the only negative matrix shift in Table II. However, attempts to assign it to other nearby states, such as $6s5d\ {}^3D_{1,2}$, result in unnaturally large matrix shifts. On similar grounds, the parity forbidden $6s5d\ {}^3D_1 \rightarrow 6s^2\ {}^1S_0$ transition is proposed to be responsible for the 24 490 cm^{-1} line.

Region 3 ($2.7 \sim 4.0 \times 10^4\ \mathrm{cm}^{-1}$). Emission lines in this region have photon energies higher than the exciting photon. We again assign the decay of various excited states according to the proximity of their wavenumber to those of excited states obtained in vacuum. Thus, the 28 857 cm^{-1} emission corresponds to $4f^{13}5d^16s^2\ (7/2, 5/2)_1$ decay; the 37 730 cm^{-1} emission corresponds to $4f^{13}5d^16s^2\ (7/2, 5/2)_1$ decay; and the 39 610 cm^{-1} emission corresponds to $4f^{13}5d^16s^2\ (7/2, 5/2)_1$ decay. The profiles of the absorption energies that populate these excited states are, respectively, peaks (c), (d), and (e) of Fig. 4. Although the matrix shift of the $6s^2\ {}^1S_0 \rightarrow 4f^{13}5d^16s^2\ (5/2, 3/2)_1$ transition appears rather large, it is comparable to the size of the matrix shift that occurs in the absorption spectrum.

IV. DISCUSSION

In order to interpret the structure of the absorption bands, we discuss here the consistency of all experimental data invoking also the results of limited theoretical simulations possible for the Yb/Ne system.

A. Stable trapping sites

The thermodynamically stable trapping sites of ground-state atomic Yb in a perfect face-centered-cubic (fcc) Ne crystals were modeled following the approach suggested in our earlier works [16,17,35–39]. The full details of the simulations are summarized in the Supplemental Material [40] to this paper. In brief, we used *ab initio* Yb($^1S_0$)-Ne [34] and slightly modified Aziz-Slaman Ne-Ne potentials [41] to represent the pairwise force field. For a large fragment of the Ne crystal, composed of more than 3000 atoms, the Yb accommodation energy $\Delta E(N)$ was obtained as a function of $N = 0, 1, \dots,\ 20$, the number of Ne atoms removed from the crystal. For each N, the lowest energy was found by minimization of the trapping site structure in configuration space and corrected by the energy required to remove N crystal atoms.

The meaningful part of the resulting $E(N)$ diagram is shown in Fig. 7. It identifies thermodynamically stable sites as those whose energies lie on its convex hull, in close analogy to the analysis of the discrete variable composition phase diagrams [42]. Four such sites are evident: the ground one, having the lowest accommodation energy, with Yb in an $N = 10$ vacancy and three others lying higher in energy with Yb in $N = 8,\ 6$, and 13 vacancies (referred to in what follows as NV for "N-atom vacancy"). Thus, the Ne crystal tends to accommodate the Yb atom in quite spacious multiple-atom vacancies. All these sites are known to be generic for the Ne fcc lattice [39]. By contrast, $N = 4$ and 6 sites compete with each other in solid Ar, an $N = 4$ site dominates in solid Kr, and a single substitutional $N = 1$ site is the most stable one in solid Xe [16]. Moreover, the energies of the perfect octahedral site, 6V, and the cuboctahedral site, 13V, are quite large, while the more energetically stable 10V and 8V sites have only axial coordination symmetries C_{4v} and C_{2v}, respectively (see Supplemental Material [40]).

As elaborated on in Secs. IV B and IV C, these findings have important implications for the CFS of the absorption bands related to $J = 1$ level excitations. In the rigid crystal environment of C_{4v} symmetry, these bands should appear as two degenerate ZPLs and a single ZPL (with associated substructures if multiple phonons are excited) according to the projection of J onto the site axis $\Omega = \pm 1$ and 0, falling into E and A_1 irreducible representations, respectively. The electron-phonon Jahn-Teller interaction should lift the remaining degeneracy, producing a 2 + 1 or 1 + 2 generic band structure, as was observed for the axial trapping site of the Ba atom [36,43,44]. For the site of C_{2v} symmetry, CFS produces three individual ZPLs.

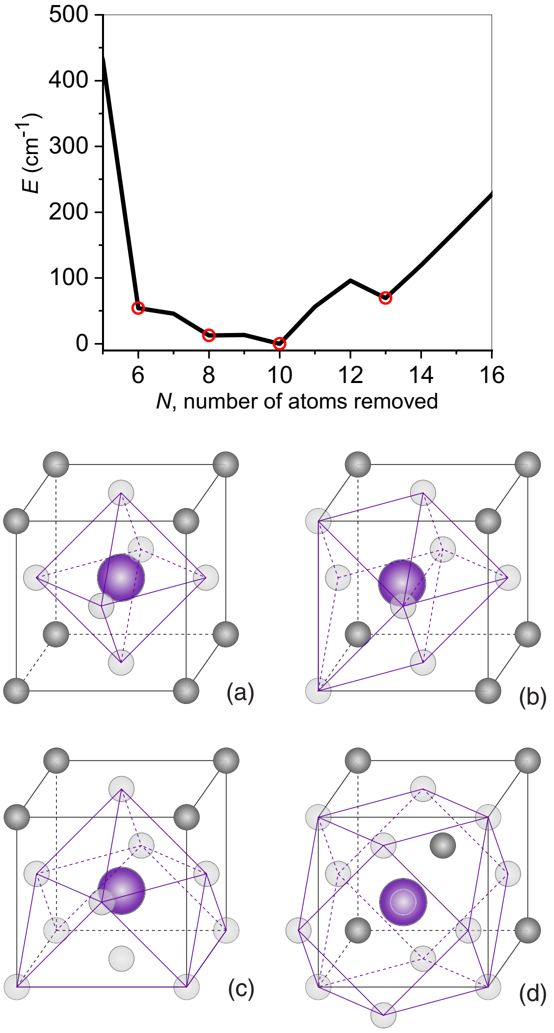

FIG. 7. Above, the accommodation energy of the Yb atom in the Ne fcc crystal as a function of N, the number of Ne atoms removed from the lattice (solid line). Red circles indicate the points lying on the convex hull of the $E(N)$ diagram. Below, the schematic structures of the Yb/Ne stable trapping sites: 6V (a), 8V (b), 10V (c), and 13V (d). Yb and Ne atoms are represented by large and small spheres, respectively; light gray spheres indicate the lattice positions of Ne atoms removed from the system; dark gray spheres indicate the lattice positions of the remaining Ne atoms.

B. $6s \rightarrow 6p$ absorption spectra

The absorption bands due to $6s \rightarrow 6p$ transitions in Figs. 4(a) and 4(b) appear as broad, weakly structured features, typical of allowed or weakly forbidden outer-electron transitions [20,43,45]. Upon $s \rightarrow p$ electron promotion, the atom-matrix interaction changes dramatically and becomes strongly anisotropic, so that multiple phonon excitations are superimposed on relatively large crystal-field splittings. At a glance, the $6s^2\ ^1S_0 \rightarrow 6s6p\ ^3P_1$ and $6s^2\ ^1S_0 \rightarrow 6s6p\ ^1P_1$ transition profiles of Figs. 4(a) and 4(b), respectively, can be interpreted as 2 + 1 and 1 + 2 split bands originating from the ground 10V site.

To verify this interpretation, we simulated the $6s \rightarrow 6p$ absorption spectra using the site geometries found for the ground state and the diatomics-in-molecule model [46–49] parametrized by the Yb($^3P_1$,$^1P_1$)-Ne *ab initio* potentials available in Ref. [34]. For the ^3P_J multiplet, we assumed a weak crystal-field limit noting that its spin-orbit coupling constant is on the order of 800 cm^{-1}, while the relative matrix-induced shifts in different types of sites do not exceed 100 cm^{-1} (Fig. 8). Further details are presented in the Supplemental Material [40] to this paper. Figure 8(a) shows the spin-orbit-coupled interaction potentials for the $^3P_1$ and $^1P_1$ atomic states. The latter state exhibits much stronger interaction anisotropy, i.e., the difference between the potentials for $\Omega = 0$ and ± 1

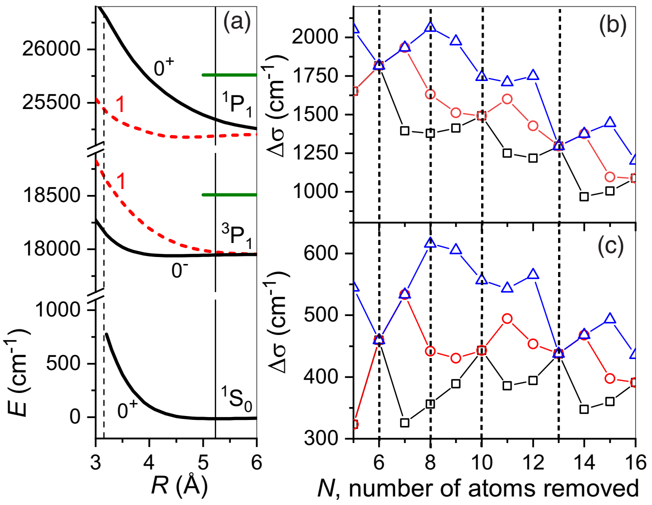

FIG. 8. (a) Yb-Ne interaction potentials for the $^3P_1$ and $^1P_1$ atomic states as functions of the internuclear distance R with Ω values indicated. The solid vertical line corresponds to the ground-state equilibrium distance, and the dashed vertical line to the Ne-Ne distance in the fcc crystal. The green horizontal bars on the right indicate the maxima of the corresponding absorption bands in Fig. 4. (b) Vertical $6s^2\,{}^1S_0 \rightarrow 6s6p\,{}^1P_1$ transition frequency shifts for the lowest-energy structures with different N. The shifts for each of the excited-state adiabatic PESs relative to the transition frequency in vacuum are represented by black squares, red circles, and blue triangles in ascending order. The vertical dashed lines indicate thermodynamically stable sites. (c) For the $6s^2\,{}^1S_0 \rightarrow 6s6p\,{}^3P_1$ transition the same is shown as for the $6s^2\,{}^1S_0 \rightarrow 6s6p\,{}^1P_1$ transition in (b).

components, than the former state. Moreover, the sign of the anisotropy for each state is the opposite of the other state's. Nevertheless, for both states, strong repulsion of one Ω component overpowers weak attraction of the other Ω component and leads to an overall positive matrix shift in their absorption frequencies.

Figures 8(b) and 8(c) present the vertical transition frequency shifts relative to the corresponding atomic transition in vacuum for the lowest-energy sites at each N. Those corresponding to the stable 6V, 8V, 10V, and 13V sites are marked by vertical lines. Three adiabatic potentials, which correlate to atomic and diatomic terms ($J = 1, \Omega$), split out differently depending on the crystal-field symmetry of the site: the polyhedral 6V and 13V sites maintain threefold degeneracy; the 10V site of C_{4v} symmetry provides a $2 + 1$ degeneracy pattern; and the 7V site of C_{3v} symmetry, which is unstable for Yb in solid Ne but stable for Ba in solid Ar, Kr, and Xe [36], produces $1 + 2$ splitting. In the sites of lower symmetries, degeneracy is completely lifted. Despite anisotropies of opposite signs, the CFS patterns of the singlet and triplet states are qualitatively similar, though the larger splittings in the case of the singlet state reflect its larger interaction anisotropy.

Molecular dynamics simulations were performed for the $6s \rightarrow 6p$ absorption band shapes, as described in the Supplemental Material [40]. Figure 9 compares the bands simulated for each stable trapping site with bands (a) and (b) of Fig. 4. The simulations systematically overestimate the matrix shift of the $6s^2\ {}^1S_0 \rightarrow 6s6p\ {}^1P_1$ absorption and, to a lesser extent, underestimate the shift of the $6s^2\ {}^1S_0 \rightarrow 6s6p\ {}^3P_1$ absorption. These errors are attributed to uncertainties in the short-range repulsive branches of the diatomic potentials, which strongly affect the transition frequencies. In agreement with the above analysis of the vertical transition frequencies, the simulated $6s^2\ {}^1S_0 \rightarrow 6s6p\ {}^1P_1$ bands are very broad and exhibit a remarkable dependence on the symmetry of the trapping site. The structures seen in their shapes fully agree with the CFS of the vertical transitions: $2 + 1$ for the 10V site with the twofold degeneracy broken by the Jahn-Teller effect; a symmetric Jahn-Teller triplet for the triply degenerate 6V site; and an asymmetric triplet for the 8V site. An unstructured asymmetric line shape is obtained for the polyhedral 13V site due to the large dynamical distortion of this spacious and labile structure. By contrast, the simulations of the $6s^2\ {}^1S_0 \rightarrow 6s6p\ {}^3P_1$ absorption predict much narrower and strongly overlapping bands. The smaller anisotropy of this state leads to smaller CFS, which is partially washed out for the 8V site. The Jahn-Teller structure is not resolved at all and only contributes to the broadening of the bands.

The simulations confirm that the observed $6s^2\ {}^1S_0 \rightarrow 6s6p\ {}^3P_1$ absorption band bears a $2 + 1$ CFS structure typical of axially symmetric sites. It may be due to occupation in a single site, most likely the 10V one, or involve contributions from the other trapping sites, which all produce bands of very similar shape, as can be seen in Fig. 9(a). Interpretation of the $^1P_1$ absorption is less obvious. Uncertainty in the excited-state Yb($^1P_1$)-Ne potentials is unlikely to be so large as to cause an inverted CFS structure for the 10V site, and we therefore explain the observed $1 + 2$ structure as a result of multiple site absorptions, which, for this particular transition, produce the distinct band shapes seen in Fig. 9(b). Attempts to fit the observed envelopes of the absorption spectrum to the weighted sum of the simulated ones gave ambiguous results. Excitation spectroscopy, which we reserve for future work,

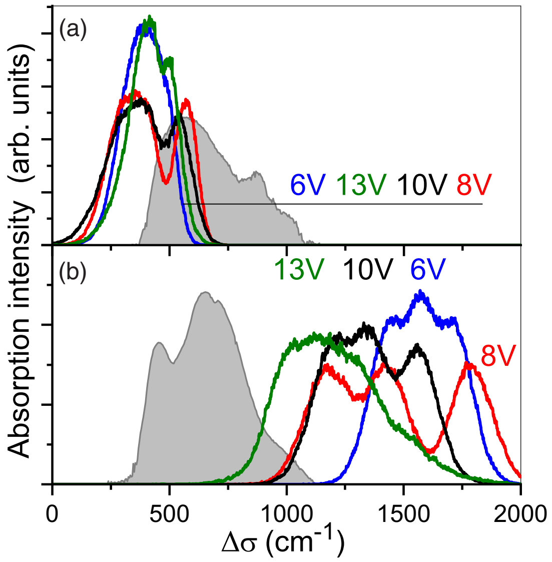

FIG. 9. Simulated and observed absorption intensities of the $^3P_1$ (a) and $^1P_1$ (b) transitions. Frequency is presented in terms of the shift relative to the atomic transition in vacuum. Each band is normalized to unit area.

is expected be more informative for the discrimination of the distinct trapping sites.

C. $4f \rightarrow 5d$ absorption spectra

The high-resolution absorption spectra of the Yb/Ne system shown in Fig. 4 exhibit a number of features that have not been previously detected in heavier RG matrices. In the latter, at low resolution, the spectra are structured in a way that reflects occupation in multiple trapping sites. Here, however, we observe much sharper structures that have qualitative similarities across all three $4f \rightarrow 5d$ absorption bands of Figs. 4(c)–4(e). As described in Sec. III A, band (c) has a low-frequency peak at 28 984 cm^{-1} and a high-frequency doublet with peaks at 29 049 and 29 073 cm^{-1}; band (e) also has a doublet, with peaks at 39 631 and 39 652 cm^{-1}, and a less resolved shoulder to its red from 39 580 to 39 610 cm^{-1}; and in band (d) the doublet has its peaks at 37 741 and 37 751 cm^{-1}. The latter band has a long harmonic progression in its red wing, which Fig. 5 shows to be especially well resolved under laser excitation. We attributed this progression to phonon sidebands and the fit presented in Sec. III B fully confirms this assignment. A more erratic secondary structure seen in band (c) may have the same origin, though the spacings between the first four peaks vary from 6 to 10 cm^{-1}.

It is extremely difficult to address the $4f^{13}5d^16s^2$ states of Yb by means of *ab initio* methods and perform quantum simulations to discern the phonon structure. Nonetheless, it is possible to make plausible inferences. First, the structure of the atomic states originating from the $4f^{13}5d^16s^2$ configuration is dominated by jj coupling and shows large spin-orbit splitting [26–28]. The weak-field approximation used for the ^3P_J multiplet should be equally valid. It is thus reasonable to attribute the overarching band structure to the $1+2$ CFS of the $J=1$ level in the axial crystal environment. As discussed above, simulations indicate that the 10V and 8V trapping sites predominate.

Second, it is well known from experiments in atomic isolation and cooling in magnetic traps and their theoretical interpretation [50,51] that interaction anisotropy of the open-shell $4f^n6s^2$ lanthanide atoms with He is strongly suppressed. As both $4f$ and $5d$ shells of the Yb atom are beneath the outer spherical $6s^2$ shell, the same suppression should be expected for the states arising from the $4f^{13}5d^16s^2$ configuration. For the same reason, the interaction potentials of these states with RG atoms should be similar to those for the $4f^{14}6s^2$ ground state. This accounts for why the peaks in Figs. 4(c)–4(e) are essentially diagonal Frank-Condon envelopes accompanied by phonon overtones. This also explains why the $1+2$ crystal-field splittings of the $4f \rightarrow 5d$ bands do not exceed 100 cm^{-1}, whereas they are ~200 and ~300 cm^{-1} for the outer-shell $6s^2\ ^1S_0 \rightarrow 6s6p\ ^3P_1$ and $6s^2\ ^1S_0 \rightarrow 6s6p\ ^1P_1$ absorptions, respectively.

Smaller $4f^{13}5d^16s^2$ state anisotropy should also diminish Jahn-Teller splitting of the doublet peaks. Observed splittings for bands (c), (d), and (e) are 25, 9, and 21 cm^{-1}, respectively. Significantly larger values of 80 and 140 cm^{-1} for bands (a) and (b), respectively, are predicted by the $6s \rightarrow 6p$ absorption simulations. Similarity of the pairs of excited- and ground-state interaction potentials in $4f \rightarrow 5d$ transitions to those in $6s \rightarrow 6p$ transitions implies similar frequencies for the phonons involved. Calculations for the 10V site simulated in Sec. IV B predict 16 and 19 cm^{-1} for A_1 and E symmetry phonons, respectively, close to the value of 14 cm^{-1} deduced from the sideband progression of A_1 symmetry phonons in Fig. 5.

D. Emission spectrum

The spectrum resulting from $6s^2\ ^1S_0 \rightarrow 6s6p\ ^1P_1$ excitation has been discussed in detail in earlier reports [11,34]. They found corroborating evidence for the presence of a crystal field in the observation of $6s6p\ ^3P_0$ state decay. The quenching of this state is posited to occur through a Stark-type coupling to the $6s6p\ ^1P_1$ and $6s6p\ ^3P_1$ states mediated by a field the order of ~20 MV/m [12]. A common feature of these reports, though, is that they only considered the fluorescence products at energies below those of the excitation energy, i.e., in the $<2.6 \times 10^4$ cm^{-1} range. This work considers the spectrum due to decay from higher-energy levels, which are reached through the absorption of a photon by the excited Yb($^3P_0$) atom. Thus, the emission counterparts to the absorption bands (c), (d), and (e) in Fig. 4 are observed at 29 030, 37 730, and 39 610 cm^{-1} in Fig. 6.

The above is important for the proposed single-atom detection of Yb in sNe [23]. The imaging of a single $ns^2\ S$ ground-state atom in RG isolation has already been demonstrated for Ba in solid Xe through the observation of the $6s6p\ ^1P_1$ state decay following its resonant excitation [24]. But efficient detection of singlet-state fluorescence is only possible when its branching ratio to other states is small. Thus, for the majority of M/RG systems, in which such fluorescence is heavily quenched by matrix-enhanced intersystem crossing, a proof-of-principle using the Yb/Ne system is highly relevant. The latter's $^3P_1$ state fluorescence has the advantage of being spectroscopically distinct from the source's exciting photons and its decay rate of ~1.47 MHz is orders of magnitude greater than the dark count rate (~25 Hz) of widely available single-photon counting modules (e.g., Perkin Elmer AQR-16 SPCM). A drawback, though, of leveraging its triplet manifold for single-atom detection is that its relatively long-lived $^3P_0$ state acts as a population trap into which electrons will be transferred on a timescale that is the order of that state's lifetime (~17 s in sNe). Fortunately, the observation here of bright $4f^{13}5d^16s^2 \rightarrow 6s^2\ ^1S_0$ fluorescence, whose decay rate is at least an order of magnitude higher than that of the $^3P_1$ state, shows that $6s6p\ ^3P_0 \rightarrow 6p^2\ ^3P_1$ repumping is a viable method for returning the dark state Yb atom back to the ground state.

An interesting feature of the Yb/Ne emission bands is their lack of complex substructure. This is particularly noticeable in the case of the $4f^{13}5d^16s^2 \rightarrow 6s^2\ ^1S_0$ decay, whose corresponding excitation profiles reflected the presence of CFS, Jahn-Teller, and electron-phonon coupling. For metal atoms isolated in the heavier RGs, structures observed in the absorption spectra due to matrix effects will usually have counterparts in the emission spectra. In sNe, however, this is rarely the case, and the literature shows the emission bands of the Zn/Ne, Cd/Ne, and Mg/Ne systems to have simple unstructured Gaussian profiles [52]. Some matrix effects can nonetheless still be resolved by lifetime measurements, as each component of the emission band may have distinct decay probabilities. Previous lifetime measurements of the Yb($^3P_0$) state in sNe were fitted to a triple exponential and the various decay constants attributed to multiple site occupation and isotope composition [11]. However, to identify such components in the lifetimes of all the excited-state decays reported here would require a significant upgrade in our apparatus and so is left for future work.

Spin polarization of ^{171}Yb nuclei in a matrix by optical pumping would enable the kinds of precision experiments envisioned for optically addressable solid-state spin systems. If the hyperfine structure of a particular transition is resolved, then it is expected that the optical pumping efficiency (the fraction of angular momentum transferred from the photon to the atom) will be high. However, if the hyperfine structure is unresolved, the optical pumping efficiency will likely depend on the details of the line-broadening mechanism. The hyperfine structure for the naturally abundant ^{171}Yb($I = 1/2$, 14%) and ^{173}Yb($I = 5/2$, 16%) isotopes do not appear to be resolved for any of the transitions studied here. This implies that the optical pumping efficiency may be low, which could be compensated for by a high number density. Because the transitions involving the inner-shell $4f$ electrons have unusually narrow features, a more detailed study of them using circularly polarized light has the potential to find evidence of optical pumping.

V. CONCLUSION

High-resolution spectroscopy of Yb atoms in a cryogenic Ne matrix over a wide excitation range revealed five asymmetric absorption features. The two lowest are assigned to outer-shell $6s \rightarrow 6p$ transitions to $6s6p^3P_1$ and $^1P_1$ atomic states and appear, respectively, as a broad doublet and an asymmetric triplet. Three bands that correspond to inner-shell $4f \rightarrow 5d$ transitions to distinct $J = 1$ states arising from the $4f^{13}5d^16s^2$ configuration are much narrower and have rich structural features.

Interpretation of the band structures relied on the modeling of the stable trapping sites of the Yb atom in a perfect Ne fcc crystal. This indicated that the most energetically stable site is a 10-atom vacancy of C_{4v} symmetry and that there are three other stable sites (6-, 8-, and 13-atom vacancies) lying relatively close by in energy. Contributions to the width of the absorption bands due to Yb occupation in the latter three sites are especially noticeable in the case of $6s \rightarrow 6p$ excitation. However, in a crystal environment in which axially symmetric occupation predominates, any $J = 1$ atomic state should be observed to split into one-dimensional A_1 and two-dimensional E representations. The dynamic Jahn-Teller effect will then lift the remaining degeneracy producing the generic $1 + 2$ or $2 + 1$ absorption band shapes observed. The magnitude of the splittings depends on the interaction anisotropy which varies from strong for the $^1P_1$ state to medium for the $^3P_1$ state and is largely suppressed for the $4f^{13}5d^16s^2$ states.

Similarly, the degree of phonon excitation reflects the difference in the ground- and excited-state interaction potentials. It ranges from significant band broadening in the $6s \rightarrow 6p$ transitions to the perfectly resolved phonon sideband progression in the $6s^2\ ^1S_0 \rightarrow 4f^{13}5d^16s^2\ (5/2, 5/2)_1$ transition. While multiple site occupation complicates the detailed assignment of all features of the $4f \rightarrow 5d$ transitions, the evidence of resolved individual phonon lines for CFS components is very strong as their fits give plausible values for the Huang-Rhys parameter and the lattice displacement.

Following the Mn/Kr [20] and Eu/Ar systems [21], the Yb/Ne system is only the third example of a metal–rare-gas matrix whose crystal-field states yield ZPLs with accompanying phonon sidebands. It is the first one for which this occurs on an allowed transition, for which sNe is the matrix host, and for which the trapping site has nonpolyhedral symmetry. These results also indicate the peculiarities of the semiquantum Ne matrix. On the one hand, well-defined CFS reflects the classical nature of relatively rigid trapping sites. On the other, the existence of multiple spacious trapping sites of axial symmetry and discernible individual phonon excitations manifest the onset of quantum solid-state physics.

ACKNOWLEDGMENTS

We would like to thank T. Oka and R. W. Dunford for helpful discussions and the use of their equipment. Experimental work and analysis is supported by Department of Energy, Office of Nuclear Physics, under Contract No. DEAC02-06CH11357, while the simulations are performed in the frame of Russian Science Foundation Project No. 17-13-01466. H.X. and S.T.P. are supported by the U.S. Department of Energy, Office of Science, Office of Basic Energy Sciences, Division of Chemical Sciences, Geosciences, and Biosciences under Contract No. DE-AC02-06CH11357. J.T.S. is supported by Argonne Director's postdoctoral fellowship and R. L. is supported by the China Postdoctoral Science Foundation.

---

[1] J. H. Van Vleck, The dipolar broadening of magnetic resonance lines in crystals, Phys. Rev. **74**, 1168 (1948).

[2] C. Kittel and E. Abrahams, Dipolar broadening of magnetic resonance lines in magnetically diluted crystals, Phys. Rev. **90**, 238 (1953).

[3] M. Arndt, S. I. Kanorsky, A. Weis, and T. W. Hänsch, Long Electronic Spin Relaxation Times of cs Atoms in Solid ^{4}he, Phys. Rev. Lett. **74**, 1359 (1995).

[4] M. G. Kozlov and A. Derevianko, Proposal for a Sensitive Search for the Electric Dipole Moment of the Electron with Matrix-Isolated Radicals, Phys. Rev. Lett. **97**, 063001 (2006).

[5] A. C. Vutha, M. Horbatsch, and E. A. Hessels, Orientation-dependent hyperfine structure of polar molecules in a rare-gas matrix: A scheme for measuring the electron electric dipole moment, Phys. Rev. A **98**, 032513 (2018).

[6] A. N. Kanagin, S. K. Regmi, P. Pathak, and J. D. Weinstein, Optical pumping of rubidium atoms frozen in solid argon, Phys. Rev. A **88**, 063404 (2013).

[7] S. Upadhyay, U. Dargyte, D. Patterson, and J. D. Weinstein, Ultralong Spin-Coherence Times for Rubidium Atoms in Solid Parahydrogen via Dynamical Decoupling, Phys. Rev. Lett. **125**, 043601 (2020).

[8] G. Wolfowicz, F. J. Heremans, C. P. Anderson, S. Kanai, H. Seo, A. Gali, G. Galli, and D. D. Awschalom, Quantum guidelines for solid-state spin defects, Nat. Rev. Mater. **6**, 906 (2021).

[9] W. Weyhmann and F. M. Pipkin, Optical absorption spectra of alkali atoms in rare-gas matrices, Phys. Rev. **137**, A490 (1965).

[10] S. Upadhyay, U. Dargyte, R. P. Prater, V. D. Dergachev, S. A. Varganov, T. V. Tscherbul, D. Patterson, and J. D. Weinstein, Enhanced spin coherence of rubidium atoms in solid parahydrogen, Phys. Rev. B **100**, 024106 (2019).

[11] C.-Y. Xu, S.-M. Hu, J. Singh, K. Bailey, Z.-T. Lu, P. Mueller, T. P. O'Connor, and U. Welp, Optical Excitation and Decay Dynamics of Ytterbium Atoms Embedded in a Solid Neon Matrix, Phys. Rev. Lett. **107**, 093001 (2011).

[12] C.-Y. Xu, J. Singh, J. C. Zappala, K. G. Bailey, M. R. Dietrich, J. P. Greene, W. Jiang, N. D. Lemke, Z.-T. Lu, P. Mueller, and T. P. O'Connor, Measurement of the Hyperfine Quenching Rate of the Clock Transition in Yb171, Phys. Rev. Lett. **113**, 033003 (2014).

[13] V. Gaire, C. S. Raman, and C. V. Parker, Subnanometer optical linewidth of thulium atoms in rare-gas crystals, Phys. Rev. A **99**, 022505 (2019).

[14] S. Upadhyay, A. N. Kanagin, C. Hartzell, T. Christy, W. P. Arnott, T. Momose, D. Patterson, and J. D. Weinstein, Longitudinal Spin Relaxation of Optically Pumped Rubidium Atoms in Solid Parahydrogen, Phys. Rev. Lett. **117**, 175301 (2016).

[15] T. E. Chupp, P. Fierlinger, M. J. Ramsey-Musolf, and J. T. Singh, Electric dipole moments of atoms, molecules, nuclei, and particles, Rev. Mod. Phys. **91**, 015001 (2019).

[16] N. N. Kleshchina, I. S. Kalinina, R. Lambo, A. A. Buchachenko, D. S. Bezrukov, and S.-M. Hu, Triplet emission of atomic ytterbium isolated in a xenon matrix, Low Temp. Phys. **45**, 707 (2019).

[17] L.-G. Tao, N. N. Kleshchina, R. Lambo, A. A. Buchachenko, X.-G. Zhou, D. S. Bezrukov, and S.-M. Hu, Heat- and light-induced transformations of Yb trapping sites in an Ar matrix, J. Chem. Phys. **143**, 174306 (2015).

[18] C. Crepin-Gilbert and A. Tramer, Photophysics of metal atoms in rare-gas complexes, clusters and matrices, Int. Rev. Phys. Chem. **18**, 485 (1999).

[19] I. B. Bersuker, *The Jahn–Teller Effect* (Cambridge University Press, Cambridge, 2006).

[20] O. Byrne, M. A. Collier, M. C. Ryan, and J. G. McCaffrey, Crystal field splitting on D↔S transitions of atomic manganese isolated in solid krypton, Low Temp. Phys. **36**, 417 (2010).

[21] O. Byrne and J. G. McCaffrey, Eu/RG absorption and excitation spectroscopy in the solid rare gases: State dependence of crystal field splitting and Jahn–Teller coupling, J. Chem. Phys. **134**, 124501 (2011).

[22] C. Cazorla and J. Boronat, Simulation and understanding of atomic and molecular quantum crystals, Rev. Mod. Phys. **89**, 035003 (2017).

[23] B. Loseth, R. Fang, D. Frisbie, K. Parzuchowski, C. Ugalde, J. Wenzl, and J. T. Singh, Detection of atomic nuclear reaction products via optical imaging, Phys. Rev. C **99**, 065805 (2019).

[24] nEXO Collaboration, Imaging individual barium atoms in solid xenon for barium tagging in nEXO, Nature (London) **569**, 203 (2019).

[25] By "absorbance" we refer to the decadic absorbance $A = -\log_{10}(1-\alpha)$. The absorbed fraction (or absorptance) is given by $\alpha = 1 - I/I_0$ with I (I_0) representing the transmitted (incident) light intensity.

[26] J.-F. Wyart and P. Camus, Extended Analysis of the Emission Spectrum of Neutral Ytterbium (Yb I), Phys. Scr. **20**, 43 (1979).

[27] R. Zinkstok, E. J. van Duijn, S. Witte, and W. Hogervorst, Hyperfine structure and isotope shift of transitions in yb i using UV and deep-UV cw laser light and the angular distribution of fluorescence radiation, J. Phys. B: At., Mol. Opt. Phys. **35**, 2693 (2002).

[28] B. Karaçoban and L. Özdemır, Energies, Landé factors, and lifetimes for some excited levels of neutral ytterbium (Z = 70), Acta Phys. Pol. A **119**, 342 (2011).

[29] S. Suzer and L. Andrews, Optical spectra of yb atoms and dimers in rare gas matrices, J. Chem. Phys. **89**, 5514 (1988).

[30] G. Liu, Advances in the theoretical understanding of photon upconversion in rare-earth activated nanophosphors, Chem. Soc. Rev. **44**, 1635 (2015).

[31] Y. Zhang, Applications of Huang–Rhys theory in semiconductor optical spectroscopy, J. Semicond. **40**, 091102 (2019).

[32] M. Wagner, Structural form of vibronic bands in crystals, J. Chem. Phys. **41**, 3939 (1964).

[33] G. Liu, A degenerate model of vibronic transitions for analyzing 4f–5d spectra, J. Lumin. **152**, 7 (2014).

[34] R. Lambo, A. A. Buchachenko, L. Wu, Y. Tan, J. Wang, Y. R. Sun, A.-W. Liu, and S.-M. Hu, Electronic spectroscopy of ytterbium in a neon matrix, J. Chem. Phys. **137**, 204315 (2012).

[35] N. N. Kleshchina, K. A. Korchagina, D. S. Bezrukov, and A. A. Buchachenko, Modeling of manganese atom and dimer isolated in solid rare gases: Structure, stability, and effect on spin coupling, J. Phys. Chem. A **121**, 2429 (2017).

[36] N. N. Kleshchina, I. S. Kalinina, I. V. Leibin, D. S. Bezrukov, and A. A. Buchachenko, Stable axially symmetric atomic impurity in an fcc solid—ba in rare gases, J. Chem. Phys. **151**, 121104 (2019).

[37] D. S. Bezrukov, N. N. Kleshchina, I. S. Kalinina, and A. A. Buchachenko, Empirically modified potentials of interaction between rare gases for matrix isolation problems, Russ. J. Phys. Chem. A **93**, 1505 (2019).

[38] A. S. Tarakanova, A. A. Buchachenko, and D. S. Bezrukov, Trapping sites of li atom in the rare gas crystals ar, kr, and xe: Analysis of stability and manifestation in the EPR spectra, Low Temp. Phys. **46**, 165 (2020).

[39] G. K. Ozerov, D. S. Bezrukov, and A. A. Buchachenko, Generic accommodations of an atom in the lennard-jones fcc and hcp rare-gas solids: A computational study, Phys. Rev. B **103**, 184110 (2021).

[40] See Supplemental Material at http://link.aps.org/supplemental/10.1103/PhysRevA.104.062809 for a description of the simulation work used to interpret the Yb/Ne absorption spectra.

[41] R. A. Aziz and M. J. Slaman, The ne-ne interatomic potential revisited, Chem. Phys. **130**, 187 (1989).

[42] Q. Zhu, L. Li, A. R. Oganov, and P. B. Allen, Evolutionary method for predicting surface reconstructions with variable stoichiometry, Phys. Rev. B **87**, 195317 (2013).

[43] B. Davis and J. G. McCaffrey, Luminescence of atomic barium in rare gas matrices: A two-dimensional excitation/emission spectroscopy study, J. Phys. Chem. A **122**, 7339 (2018).

[44] B. M. Davis, B. Gervais, and J. G. McCaffrey, An investigation of the sites occupied by atomic barium in solid xenon—A 2D-EE luminescence spectroscopy and molecular dynamics study, J. Chem. Phys. **148**, 124308 (2018).

[45] B. M. Davis and J. G. McCaffrey, Aborption spectroscopy of heavy alkaline earth metals Ba and Sr in rare gas matrices—CCSD(T) calculations and atomic site occupancies, J. Chem. Phys. **144**, 044308 (2016).

[46] M. Ryan, M. Collier, P. de Pujo, C. Crépin, and J. G. McCaffrey, Investigations of the optical spectroscopy of atomic sodium isolated in solid argon and krypton: Experiments and simulations, J. Phys. Chem. A **114**, 3011 (2009).

[47] J. A. Boatz and M. E. Fajardo, Monte Carlo simulations of the structures and optical absorption spectra of Na atoms in Ar clusters, surfaces, and solids, J. Chem. Phys. **101**, 3472 (1994).

[48] J. P. Visticot, P. de Pujo, J. M. Mestdagh, A. Lallement, J. Berlande, O. Sublemontier, P. Meynadier, and J. Cuvellier, Experiment versus molecular dynamics simulation: Spectroscopy of Ba–(Ar)n clusters, J. Chem. Phys. **100**, 158 (1994).

[49] A. I. Krylov, R. B. Gerber, and R. D. Coalson, Nonadiabatic dynamics and electronic energy relaxation of cl(2p) atoms in solid Ar, J. Chem. Phys. **105**, 4626 (1996).

[50] C. I. Hancox, S. C. Doret, M. T. Hummon, L. Luo, and J. M. Doyle, Magnetic trapping of rare-earth atoms at millikelvin temperatures, Nature (London) **431**, 281 (2004).

[51] R. V. Krems and A. A. Buchachenko, Electronic interaction anisotropy between open-shell lanthanide atoms and helium from cold collision experiment, J. Chem. Phys. **123**, 101101 (2005).

[52] B. Healy, P. Kerins, and J. G. McCaffrey, Metal atom (Zn, Cd and Mg) luminescence in solid neon, Low Temp. Phys. **38**, 679 (2012).